PHYSICAL REVIEW A **110**, 013309 (2024)

Ultracold-molecule higher-order topological phases induced by long-range dipolar interactions in optical-tweezer lattices

Jinzhu Jiang, Zhonghua Ji,[*] Feng Mei,[†] Jie Ma, Liantuan Xiao, and Suotang Jia
State Key Laboratory of Quantum Optics and Quantum Optics Devices, Institute of Laser Spectroscopy, Shanxi University, Taiyuan, Shanxi 030006, China
and Collaborative Innovation Center of Extreme Optics, Shanxi University, Taiyuan, Shanxi 030006, China

(Received 6 November 2023; revised 24 June 2024; accepted 25 June 2024; published 11 July 2024)

Ultracold atomic and molecular systems in the past years have significantly advanced the exploration of topological phases of matter. Notably, the recent experimental progress achieved in ultracold molecules, particularly within optical-tweezer lattices and leveraging long-range dipolar interactions, has opened up new avenues for this prospect. Here, we propose the creation of an ultracold-molecule trimerized Kagome optical-tweezer lattice to examine the topological phases induced by long-range dipolar interactions. Through a comparison of topological features in scenarios with and without long-range couplings, we find that the long-range interactions can induce higher-order topological phases with diverse topological corner modes at each corner, a phenomenon that can even emerge in nonstandard trimerized Kagome lattices. Furthermore, we develop a dynamic method to spectrally and spatially detect these topological corner modes. Our research not only underscores that long-range interactions can engender much richer topological phases but also suggests exciting possibilities for designing reconfigurable topological lattices.

DOI: 10.1103/PhysRevA.110.013309

I. INTRODUCTION

Ultracold atoms trapped in optical lattices have emerged as versatile platforms for implementing and investigating topological phases of matter [1–3]. These systems enable the realization of various fundamental topological phases, starting from the generation of synthetic spin-orbit couplings [4–16] and gauge fields [17–19]. Among the achieved phases are chiral topological insulator phases [20–26], integer quantum Hall phases [27], Chern insulator phases [28–30], topological nodal lines [31], Weyl semimetal phases [32], and even Floquet topological phases [33–36]. The inherent access to momentum spaces in ultracold-atom optical lattice setups allows for the direct detection of bulk topological features [37–39]. However, current systems encounter limitations in fully exploring topological phases, notably in implementing long-range couplings to reveal richer topological features and in creating open-boundary conditions to study landmarked topological boundary states.

In parallel, significant progress has been made in the quantum preparation and manipulation of ultracold molecules within optical tweezer arrays over the past five years [40–64]. In contrast to ultracold atoms, ultracold-molecule systems possess unique characteristics, including rich internal structures and long-range dipolar interactions. Consequently, they offer new avenues for applications in quantum computation [65–71], quantum simulation [72–81], quantum chemistry [82–86], and precision measurements [87,88]. Notably, recent experimental breakthroughs have demonstrated quantum entanglement generation between two ultracold molecules trapped in optical tweezers [89,90].

Programmable optical-tweezer lattices of ultracold molecules also hold promise for implementing topological phases of matter, including topological flat bands [91,92], fractional Chern insulators [93], Weyl excitations [94], Hopf topological insulators [95,96], and symmetry-protected topological phases [97]. As demonstrated in a very recent experiment, leveraging the optical-tweezer lattice naturally with open boundaries, topological boundary states are directly observed in a one-dimensional optical-tweezer lattice [98]. This feature also provides a convenient way to probe the fractional topological numbers associated with the topological boundary [99,100] or defect states [101]. Notably, while previous investigations into ultracold-molecule topological phases have focused on nearest-neighbor couplings, the presence of long-range dipolar interactions in ultracold molecules calls for exploration of the topological features induced by such interactions, a capability beyond the reach of ultracold-atom platforms.

In this paper, we explore higher-order topological phases (HOTPs) of ultracold molecules induced by long-range dipolar interactions within an optical-tweezer lattice. Unlike previously studied topological phases, HOTPs have recently garnered significant interest [102–107], as they feature topological boundary states at lower-dimensional boundaries that go beyond the standard bulk-boundary correspondence. However, existing studies often overlook the long-range couplings. Our research underscores the importance of considering these interactions, as shown below they can give rise to new HOTPs.

---

[*] Contact author: jzh@sxu.edu.cn

[†] Contact author: meifeng@sxu.edu.cn

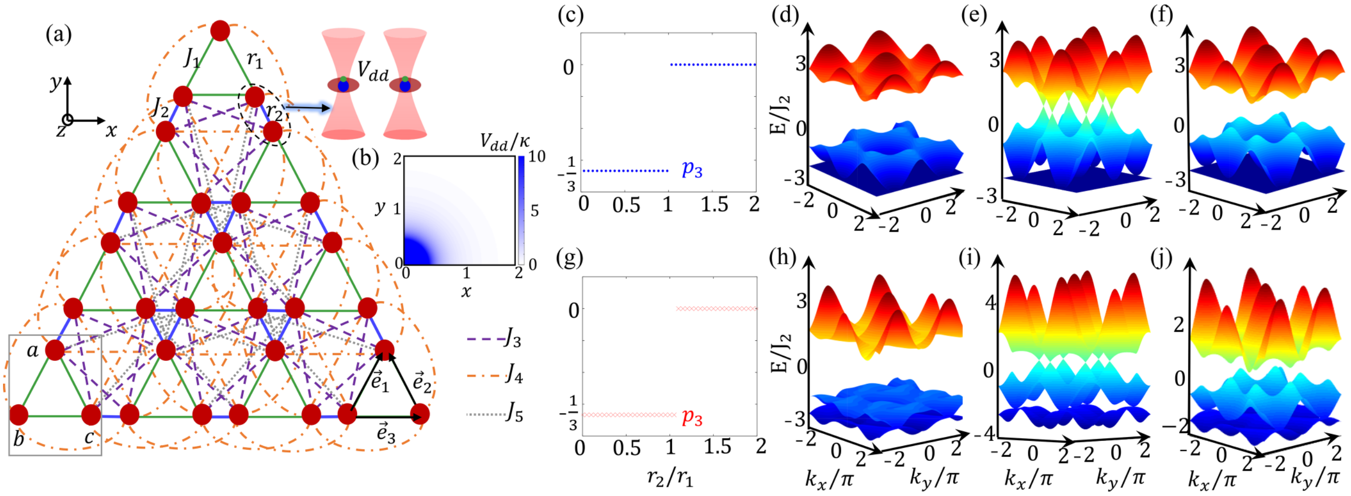

FIG. 1. (a) Schematic of trimerized Kagome molecule lattice created by optical tweezers with long-range dipolar interactions. The separation distances r_1 and r_2 are controlled by reconfiguring the tweezer positions, enabling us to tune the dipolar interaction strengths. Panel (b) shows the geometric factor J_{ij}/V_0 between the origin and (x, y). Polarization p_3 for the third band as a function of r_2/r_1 for the system (c) without long-range couplings and (g) with long-range couplings. The occurrences of topological phase transitions are signified by the jumps of p_3 at (c) $r_2/r_1 = 1$ and (g) $r_2/r_1 = 1.1$, as manifested by the gap-closing processes respectively in panels [(d)–(f)] and panels [(h)–(j)]. The parameters are as follows: (d, h) $r_2/r_1 = 0.7$, (e) $r_2/r_1 = 1$, (i) $r_2/r_1 = 1.1$, and (f, j) $r_2/r_1 = 1.2$.

Specifically, we investigate ultracold molecules confined in a trimerized optical tweezer Kagome lattice, which can be easily fabricated by leveraging the reconfigurable nature of optical tweezers. Through calculations of band polarizations and open-boundary-condition (OBC) energy spectra, we examine the higher-order topological characteristics in both the absence and the presence of long-range couplings. Interestingly, we find that incorporating long-range couplings can induce novel higher-order topological phases, characterized by multiple diverse topological corner modes at each corner.

Furthermore, we introduce a method for detecting the local density of states (LDOS) of the ultracold molecular lattice. Notably, the LDOS measurement technique commonly used in electronic systems cannot be applied to ultracold-molecule systems. This progress enables us to spectroscopically and spatially probe both the topological corner and the edge modes. Our LDOS detection method is also adaptable for use in ultracold-atom systems, thereby offering a versatile probing tool for the field of synthetic ultracold topological phases. Moreover, we also find that the numbers of topological corner modes induced by long-range couplings can be significantly larger in an extended Kagome lattice. This underscores the potency and versatility of long-range dipolar interactions and reconfigurable optical-tweezer lattices in implementing and exploring topological phases of matter.

The paper is organized as follows. Section II presents the higher-order topological features of ultracold-molecule trimerized Kagome optical-tweezer lattice, including the topological band polarizations and corner modes and the topological LDOS detection. Section III investigates the case in a generalized Kagome lattice with larger numbers of topological corner modes. Section IV gives a summary and outlook for this paper.

II. HOTPS IN ULTRACOLD-MOLECULE TRIMERIZED KAGOME OPTICAL-TWEEZER LATTICES

A. Trimerized Kagome optical-tweezer lattices

We consider ultracold polar molecules trapped in a trimerized Kagome optical-tweezer lattice, as illustrated in Fig. 1(a), along three directions which has an alternative J_1-J_2 coupling configuration. The molecular species can be NaCs or CaF, which both have been trapped in optical-tweezer arrays. The dipole-dipole interaction Hamiltonian between molecules reads

$$H_{dd} = \frac{1}{2}\sum_{i\neq j}\frac{\kappa}{R_{ij}^3}[\mathbf{d}_i\cdot\mathbf{d}_j - 3(\mathbf{d}_i\cdot\mathbf{R}_{ij})(\mathbf{d}_j\cdot\mathbf{R}_{ij})], \quad (1)$$

where $\kappa = 1/4\pi\varepsilon_0$, $\mathbf{d}_i$ is the dipole moment of molecule i, and $\mathbf{R}_{ij}$ is the vector connecting the two molecules i and j. In the spherical coordinates and in terms of spherical tensors, the long-range dipolar interaction can be further written as

$$H_{dd} = -\frac{\sqrt{6}}{2}\sum_{i\neq j}\frac{\kappa}{R_{ij}^3}\sum_{p=-2}^{2}(-1)^p C^2_{-p}(\theta,\phi)T^2_p(\mathbf{d}_i,\mathbf{d}_j), \quad (2)$$

where $C^2_{-p}(\theta,\phi) = \sqrt{\frac{4\pi}{5}}Y_{2,-p}(\theta,\phi)$ and the spherical tensors are given by $T^2_{\pm 1} = (d_i^z d_j^{\pm} + d_i^{\pm} d_j^z)/\sqrt{2}$, $T^2_{\pm 2} = d_i^{\pm} d_j^{\pm}$, $T^2_0 = (d_i^- d_j^+ + 2d_i^z d_j^z + d_i^+ d_j^-)/\sqrt{6}$. Here, (θ, ϕ) are the spherical coordinates of $\mathbf{R}_{ij}$ in the molecule coordinate frame. The quantization axis setting by external magnetic fields is perpendicular to the x-y plane where molecules stay in, as shown in Fig. 1(a); thus, the angle between the quantization axis and $\mathbf{R}_{ij}$ is $\theta = \pi/2$.

Suppose each molecule is a spin one-half. The spin-up and spin-down are encoded by two molecular rotational states, i.e., $|\uparrow\rangle = |0, 0\rangle$ and $|\downarrow\rangle = |1, -1\rangle$. In the absence of electric fields, by projecting the Hamiltonian H_{dd} into the Hilbert space spanned by $\{|\uparrow\rangle, |\downarrow\rangle\}$, we obtain a long-range spin-exchange interaction Hamiltonian:

$$H = \sum_{i>j} J_{ij}(S_i^+ S_j^- + S_i^- S_j^+), \tag{3}$$

where S_i^+ is the spin-raising operator of the molecule at the lattice site i, and J_{ij} is the distance-dependent long-range spin-exchange interaction strength,

$$J_{ij} = \frac{V_0}{R_{ij}^3}, \tag{4}$$

where $V_0 = -\kappa d_{\uparrow\downarrow}^2/2$ and $d_{\uparrow\downarrow} = \langle\uparrow|d^+|\downarrow\rangle$ is the transition dipole moment.

As a result, in addition to the nearest-neighbor spin-exchange couplings $J_{1,2}$, the trimerized Kagome lattice also exhibits long-range couplings. Figure 1(b) examines the variation of the geometric factor $1/R_{ij}^3$ with the increase of R_{ij}. It is evident that this factor rapidly decreases to zero, suggesting that beyond a certain range the long-range couplings become negligible. For the trimerized Kagome geometry, our calculations indicate that, compared to $J_{1,2}$, the long-range couplings beyond $J_{3,4,5}$ are very small, at least on the order of 10^{-2}, and their influence on the topological properties is minor. Consequently, the long-range couplings considered in our study are limited to $J_{3,4,5}$. Moreover, all the spin-exchange coupling strengths are correlated with each other through the distance ratio r_2/r_1. Specifically, $J_{1,2,3,4,5}$ vary with $r_{1,2}$ as given by

$$J_1 = \frac{V_0}{r_1^3}, \quad J_2 = \frac{V_0}{r_2^3}, \quad J_4 = \frac{V_0}{(r_1+r_2)^3},$$
$$J_3 = \frac{V_0}{\left(\sqrt{r_1^2 + r_2^2 + r_1 r_2}\right)^3},$$
$$J_5 = \frac{V_0}{\left[\sqrt{(r_1+r_2)^2 + r_2^2 + (r_1+r_2)r_2}\right]^3}. \tag{5}$$

Therefore, the topological properties for the long-range trimerized kagome lattice are determined by r_2/r_1, which can be easily tuned by moving optical tweezers.

B. Higher-order topological phases induced by long-range interactions

1. *Bulk topology characterization*

We employ bulk polarization to characterize the bulk topology of the trimerized Kagome lattice within the single spin-up excitation subspace. Since the trimerized Kagome lattice in Fig. 1(a) adheres to C_3 rotation symmetry, the bulk polarization value can be derived from the eigenvalue of C_3 symmetry at the C_3-invariant point K [105–107]. This takes the following form:

$$2\pi p_n = \arg\theta_n(K) (\mathrm{mod}\, 2\pi), \tag{6}$$

where $\theta_n(k) = \langle u_{k,n}|R_3|u_{k,n}\rangle$, with $|u_{k,n}\rangle$ being the Bloch wave function of the nth energy band and R_3 being the C_3 rotation symmetry operator (see the Appendix). The C_3 rotation symmetry leads to quantized values of p_n as $p_n = \frac{l}{3}$ ($l = 0$ and ±1) [105–107]. As depicted in Figs. 1(d)–1(f), as J_2/J_1 varies, the upper gap (between the first and second bands) experiences a closing-reopening process. Notably, the third band is a flat band arising from the specific geometric arrangement and symmetry of the lattice couplings. In contrast, the lower gap (between the second and third bands) remains closed, which is guaranteed by the C_3 rotational symmetry of the lattice. Consequently, we focus on examining the changes in topological features associated with the upper gap. To this end, we utilize the polarization of the third band [the upper band in Figs. 1(d)–1(f)] as a topological index to characterize the higher-order topological features. In the absence of long-range interactions, the polarization is obtained in Fig. 1(c),

$$p_3 = \begin{cases} -\frac{1}{3}, & r_2/r_1 < 1, \\ 0, & r_2/r_1 > 1, \end{cases} \tag{7}$$

where the fractional quantization value identifies that the corresponding system is in the nontrivial HOTPs. Notice that the zero value of r_2/r_1 means that r_1 is much bigger than r_2. In practical experiments, it is quite challenging to tune the system into the configuration with $r_2 = 0$. The jump of p_3 to zero occurs at $r_2/r_1 = 1$, signifying the occurrence of topological phase transition, which is always accompanied by a band gap closing. As demonstrated in Figs. 1(d)–1(f), the energy gap closing between the third and second bands takes places at $r_2/r_1 = 1$, agreeing with the topological phase transition point. In contrast, in the presence of long-range interactions [Fig. 1(g)], the quantization is calculated as

$$p_3 = \begin{cases} -\frac{1}{3}, & r_2/r_1 < 1.1, \\ 0, & r_2/r_1 > 1.1. \end{cases} \tag{8}$$

As shown, the long-range interaction can shift the topological phase transition point to $r_2/r_1 = 1.1$. This is also manifested in Figs. 1(h)–1(j) by the shift of the gap-closing point. Meanwhile, we also notice that the presence of long-range couplings breaks the flat band condition and turns the third band into a dispersive band. In addition to the bulk topological feature, in the following section, we demonstrate the long-range interaction can induce the emergence of new topological corner modes.

2. *Topological corner modes*

Bulk-edge correspondence is a basic theorem associated with topological phases. The nontrivial fractional quantized topological bulk polarization guarantees the emergence of topological corner modes in the upper gap at the corners of the trimerized Kagome lattice. To demonstrate this point, Fig. 2(a) is a study of the energy spectrum of the system within the single spin-up excitation subspace in the absence of long-range couplings under the open-boundary condition. As shown, for $r_2/r_1 < 1$, there emerges threefold degenerate zero-energy topological modes in the lower gap, dictated and protected by the nontrivial fractional quantized $p_3 = -\frac{1}{3}$ in Fig. 1(c). Specifically, Fig. 2(b) exhibits the OBC energy spectrum for $r_2/r_1 = 0.5$. Besides the in-gap zero-energy type I corner modes (A), edge modes (B and C) also exist, with their spatial distributions displayed in Figs. 2(c)–2(e). As indicated, the zero-energy modes correspond to topological corner modes maximally distributed at the three outside corners [Fig. 2(c)],

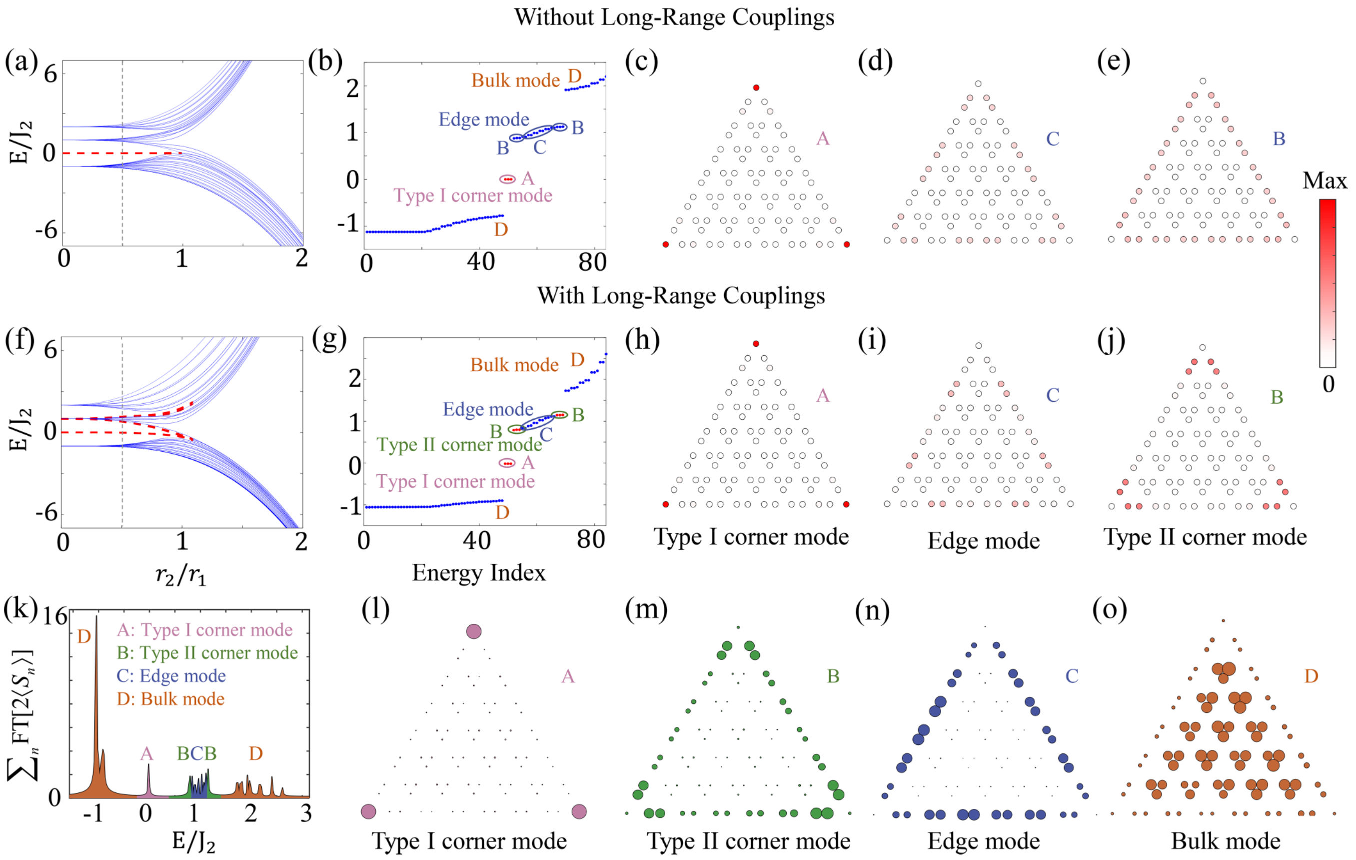

FIG. 2. (a) OBC energy spectrum of an 84-molecule trimerized Kagome lattice as a function of r_2/r_1 without long-range couplings. (b) The specific OBC energy spectrum for $r_2/r_1 = 0.5$. A and D respectively mark the type I corner and bulk modes. B and C respectively mark the edge modes at the edges and the interior of edge bands. [(c)–(e)] Spatial distributions of the modes respectively in A, C, and B. [(f)–(j)] Same as panels [(a)–(e)] but with long-range couplings. In contrast, here B becomes the type II corner modes induced by long-range interactions. (k) Sum of the LDOS over all lattice sites, with long-range couplings. [(l)–(o)] Spatial distributions of LDOS integrated over an energy range respectively covering the type I and type II corner modes, the edge bands, and the bulk bands. Each site is represented as a circle with a radius proportional to the LDOS. The parameter is $r_2/r_1 = 0.5$. We assume 3% disorders in all couplings for showing the robustness.

and the modes in B and C correspond to the edge modes maximally populating the three edges [Figs. 2(d) and 2(e)].

In contrast, Figs. 2(f)–2(j) examine the scenario when long-range couplings are present. First, it is observed that the point at which the zero-energy modes intersect with the bulk modes shifts from $r_2/r_1 = 1$ [Fig. 2(a)] to $r_2/r_1 = 1.1$ [Fig. 2(f)], a consequence of the influence of long-range interactions, consistent with the earlier predictions based on the bulk polarization depicted in Fig. 1(g). Second, it is noted that in the presence of long-range interactions, the six edge modes in B depicted in Fig. 2(b) transform into the corner modes showcased in Fig. 2(g), primarily distributed at the three internal corners illustrated in Fig. 2(j). Throughout this study, we denote these modes as type II corner modes. In both cases, with or without long-range couplings, for the modes in the three bulk bands, their real-space wave functions are all extended states and are homogeneously distributed at the insider bulk sites, as manifested by the LDOS in Fig. 2(o).

3. Topological LDOS detection

In this work, we introduce an experimentally accessible method to detect the LDOS associated with the ultracold-molecule trimerized Kagome lattice, which allows us to directly measure the OBC energy spectrum and spatial distributions of corner modes. Suppose the lattice contains N tweezers. Initially, all the molecules in the tweezers are prepared into the state

$$\begin{aligned}|\psi_n\rangle &= |\downarrow_1\rangle|\downarrow_2\rangle\cdots\left(\frac{|\downarrow\rangle+|\uparrow\rangle}{\sqrt{2}}\right)\cdots|\downarrow_{N-1}\rangle|\downarrow_N\rangle\\ &= \frac{1}{\sqrt{2}}(|G\rangle+|\uparrow_n\rangle),\end{aligned} \tag{9}$$

where $|G\rangle$ represents the ground state, with all molecules staying in the spin-down state, and $|\uparrow_n\rangle$ represents a molecular spin-up excitation placed on the lattice site n. After subsequent time evolution, the state becomes

$$|\psi(t)\rangle = |G\rangle + \sum_\alpha C_{n,\alpha}e^{-iE_\alpha t/\hbar}|\phi_\alpha\rangle, \tag{10}$$

where E_α is the eigenenergy of the trimerized Kagome lattice, $|\phi_\alpha\rangle$ is the corresponding eigenstate, and $C_{n,\alpha}$ is the amplitude of the single spin-up excitation state projected into the eigenstate $\langle\psi_\alpha|\uparrow_n\rangle$.

Such a dynamical response is detected by measuring the time evolutions of $\langle S_{x,y}(t)\rangle$. Then, we can get an experimentally measurable observable,

$$\langle S_n(t)\rangle = \sum_{\alpha} \frac{|C_{n,\alpha}|^2}{2} e^{-iE_\alpha t}, \tag{11}$$

where $\langle S_n\rangle = (\langle S_n^X\rangle + i\langle S_n^Y\rangle)/2$. After that, based on a Fourier transformation, we obtain a relationship between the LDOS at the lattice site n and the observable $\langle S_n\rangle$,

$$\rho(n, E_\alpha) = \mathrm{FT}[2\langle S_n\rangle]. \tag{12}$$

By repeating this procedure and running n from 1 to N, every energy eigenstate is ensured to have some overlap with one of the initial single spin-up excitation states, thus the LDOS of all sites can be detected.

Figure 2(k) presents the sum of the LDOS $\rho(n, E_\alpha)$ over all lattice sites, i.e., the DOS. As shown, the distinct peaks directly measure out the OBC energy spectrum in Fig. 2(g) with long-range couplings, including pinpointing the location of the zero-energy type I corner modes and the edge bands. On the other hand, the integrations of the LDOS over an energy range containing the corner, edge, and bulk modes can precisely detect their spatial distributions, as illustrated in Figs. 2(l)–2(o). As revealed, besides the type I corner modes [labeled by A in Fig. 2(k)], the edge modes (C), and the bulk modes (D), there also emerge type II corner modes (B), as a result of long-range couplings. Due to the finite-size effect, the type II corner modes are hybridized with the edge modes. As a result, in addition to the corner-dominated LDOS in Fig. 2(m), there also exists considerable LDOS in the edges. However, we still can robustly distinguish the B and C modes by determining whether the modes are dominantly localized at the corner or simultaneously maximally localized at the edge sites. This distinction could become more evident by using a larger lattice size.

4. Dynamical detection of topological corner modes

Molecular topological corner modes can also be detected by spin dynamics. First, we show how to detect the type I corner mode. To detect such a corner mode, the system is initialized into the single spin-up excitation state $|\psi(t=0)\rangle = |\uparrow\downarrow\cdots\downarrow\downarrow\rangle$, with the single molecules trapped at the upper corner tweezer flipped into the spin-up state, as illustrated in Figs. 3(a) and 3(d). The time evolution for such an initial state is described by $|\psi(t)\rangle = e^{-iHt}|\psi(t=0)\rangle$. For the trimerized Kagome lattice in the nontrivial HOTPs, according to the spatial distribution feature of the type I corner mode [Figs. 3(a)–(c)], such an initial state would have a large overlap with the wave function of the type I corner mode, making such a mode be excited. As a result, the time evolution of $|\psi(t=0)\rangle$ is mainly governed by the type I corner mode. As manifested in Figs. 3(b) and 3(c), the dynamics of the spin-up density is maximally distributed at the upper corner tweezer. While for the time evolutions in trivial HOTPs [in Figs. 3(d)–3(f)], such an initial corner-excited state would evolve into the bulk of the lattice, resulting in there being no corner modes in this case. In a similar way, as exhibited in Figs. 3(g)–3(l), by motioning the time evolutions of spin-up excitation initially placed on the type II corner tweezer, one can detect the existence of type II corner modes.

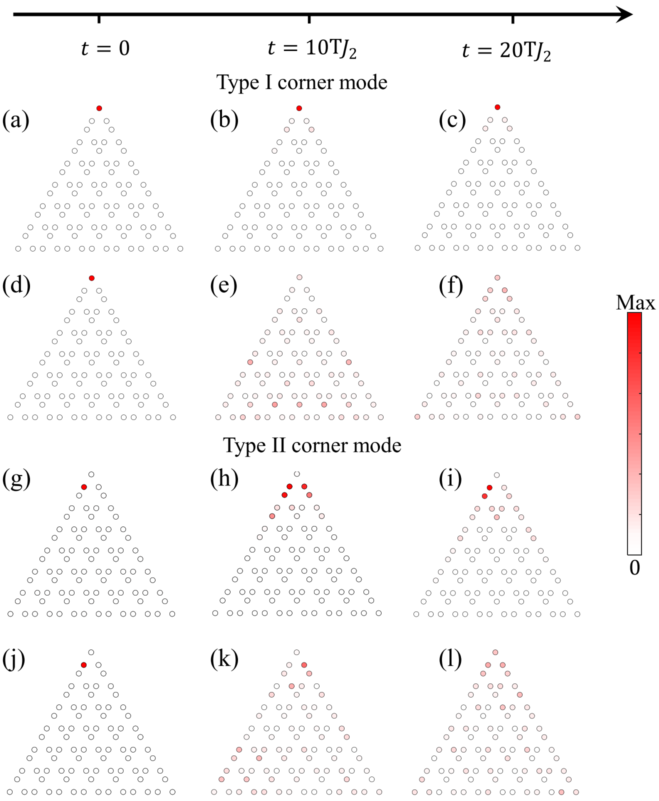

FIG. 3. The single molecules at the (a), (d) type I corner tweezers are initially excited into the spin-up states. After subsequent time evolutions, spin-up density distributions for the lattice in nontrivial [panels (a)–(c)] and trivial [panels (d)–(f)] HOTPs, at (b), (e) $t = 10/J_2$ and (c), (f) $t = 20/J_2$. [(g)–(l)] Same as panels [(a)–(f)] but for initially exciting (g), (j) type II corner tweezers, with panels [(g)–(i)] and [(j)–(l)] respectively corresponding to the nontrivial and trivial cases. The parameter is $r_2/r_1 = 0.5$. We assume 3% disorders in all couplings for showing robustness.

As shown, compared with the LDOS method, the experimental technology requirements for the dynamical detection method are much simpler than those for the LDOS detection method. However, the LDOS method provides deeper insights into topological features. It not only detects localization features like the dynamical method but also reveals the internal spatial structure, such as which corner sites are predominantly populated by corner modes. Moreover, the LDOS method can also probe the spectral features of the corner modes, uncovering their topological spectral characteristics.

III. HOTPS IN EXTENDED ULTRACOLD-MOLECULE TRIMERIZED KAGOME LATTICES

A. Extended ultracold-molecule trimerized Kagome lattices

In this section, we further show that HOTPs induced by long-range interactions can even emerge in a nonstandard Kagome lattice. Specifically, as depicted in Fig. 4(a), we generalize the unit cell of the above-studied standard Kagome lattice to contain four sites. In addition to the nearest-neighbor couplings $J_{1,2}$, there are also the long-range couplings $J_{3,4,5}$,

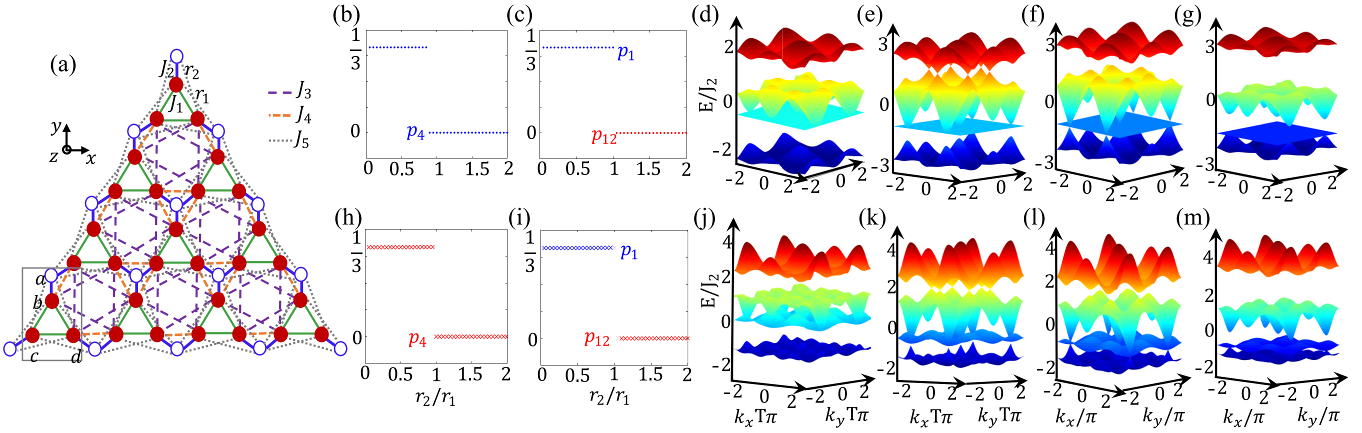

FIG. 4. (a) Schematic of extended trimerized kagome molecule tweezer lattice, featuring four tweezers in each unit cell. Polarizations (b), (h) p_4 and (c), (i) $p_{1,12}$ respectively characterizing the topology of the upper and lower energy gaps, as a function of r_2/r_1, for the system (b), (c) without and (h), (i) with long-range couplings. Topological phase transitions occur as p_4 and $p_{1,12}$ jump at (b) $r_2/r_1 = 0.89$, (h) $r_2/r_1 = 0.95$, and (c), (i) $r_2/r_1 = 1$, as evidenced by the gap-closing processes in panels [(d)–(g)] and [(j)–(m)], respectively. The parameters are (d), (j) $r_2/r_1 = 0.7$, (e) $r_2/r_1 = 0.89$, (k) $r_2/r_1 = 0.95$, (f), (l) $r_2/r_1 = 1$, and (g), (m) $r_2/r_1 = 1.2$.

given by

$$J_1 = \frac{V_0}{r_1^3},\quad J_2 = \frac{V_0}{r_2^3},\quad J_4 = \frac{V_0}{(\sqrt{3}r_2)^3},$$
$$J_3 = \frac{V_0}{\left[\sqrt{r_1^2 + (\sqrt{3}r_2)^2 + \sqrt{3}r_1 r_2}\right]^3},$$
$$J_5 = \frac{V_0}{\left(\sqrt{r_1^2 + r_2^2 + \sqrt{3}r_1 r_2}\right)^3}. \tag{13}$$

Compared to $J_{3,4,5}$, the much-longer-range couplings are very small, at least on the order of 10^{-2}, which can be safely ignored.

B. Higher-order topological phases induced by long-range interactions

1. Bulk topology characterization

As shown in Fig. 4(a), the extended ultracold-molecule kagome lattice also satisfies C_3 rotation symmetry. As a consequence, its bulk topology can also be characterized by band polarizations. According to Figs. 4(d)–4(g), we can see that there are two gap-closing points, corresponding to the upper and lower gap closings, respectively shown in Figs. 4(e) and 4(f). To identify the change of topological phase transition associated with the upper gap-closing process, we calculate the polarization of the fourth band p_4. While for the lower gap, before the gap closing, its topology can be identified by the polarization of the first band p_1. After the gap closing, the first and second bands feature degeneracy, and the topology of the corresponding lower gap is characterized by a non-Abelian polarization [105–107],

$$2\pi p_{12} = \arg\left[\det \Xi(\mathrm{K})\right](\mathrm{mod}\, 2\pi), \tag{14}$$

where $\Xi_{i,j}(k) = \langle u_{k,i}|R_4|u_{k,j}\rangle (i, j \in 1, 2)$, with R_4 being the rotation symmetry operator. In the absence of long-range couplings, Fig. 4(b) shows that the polarization p_4 is calculated as

$$p_4 = \begin{cases} \frac{1}{3}, & r_2/r_1 < 0.89, \\ 0, & r_2/r_1 > 0.89. \end{cases} \tag{15}$$

The jump signifies the occurrence of topological phase transition at $r_2/r_1 = 0.89$, agreeing with the point where the upper gap closes, as shown in Fig. 4(e). The polarization p_4 in the presence of long-range couplings is numerically calculated in Fig. 4(h), giving

$$p_4 = \begin{cases} \frac{1}{3}, & r_2/r_1 < 0.95, \\ 0, & r_2/r_1 > 0.95. \end{cases} \tag{16}$$

As indicated, the topological phase transition point is changed to $r_2/r_1 = 0.95$ due to long-range couplings, which is also in agreement with the upper gap-closing point in Fig. 4(k). While for the topology of the lower gap, from the calculated polarizations $p_{1,12}$ [Figs. 4(c) and 4(i)], we can see that the topological phase transition point remains at $r_2/r_1 = 1$ in the presence of long-range couplings. This feature is further verified in Figs. 4(f) and 4(l) in which the lower gap-closing points coincide at $r_2/r_1 = 1$. Notably, according to bulk-boundary correspondence, the nontrivial fractional quantized polarization value identifies that this gap is topologically nontrivial, ensuring the emergence of topological corner modes in this gap.

2. Topological corner modes and LDOS detection

In this section, we demonstrate that long-range couplings also can induce topological corner modes in the nonstandard Kagome lattice, which also can be detected by the LDOS approach. Specifically, Fig. 5(a) investigates the OBC energy spectrum in the absence of long-range couplings. As shown, for $r_2/r_1 < 0.89$ (1), there emerge topological corner modes in the upper (lower) gap. By examining the case of $r_2/r_1 = 0.58$ [Fig. 5(b)], we can further see that, besides the three bulk bands, there are two edge bands and six type I corner modes, as manifested by their spatial distributions in Figs. 5(c)–5(e). In particular, the type I corner modes are maximally

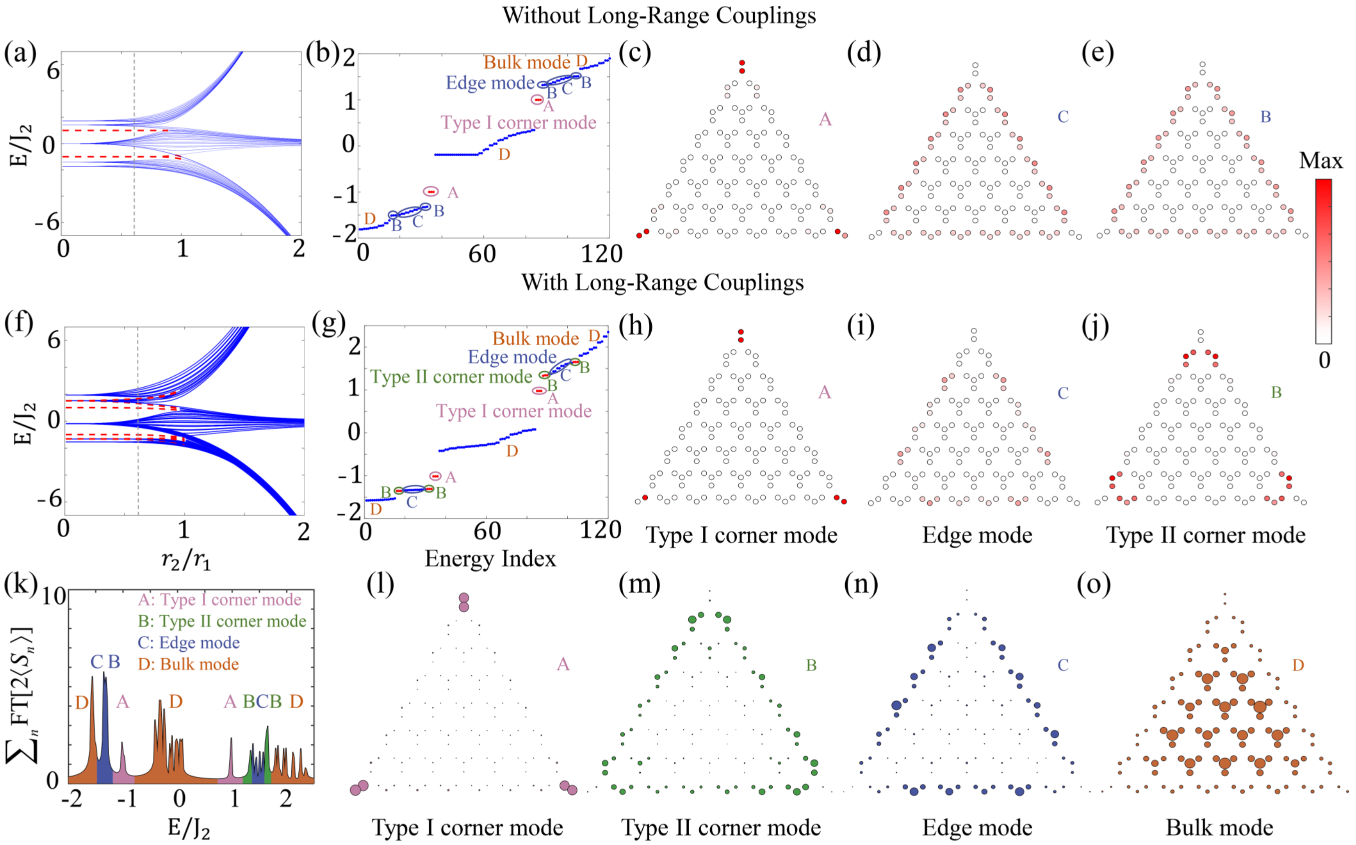

FIG. 5. (a) OBC energy spectrum of a 120-molecule extended trimerized Kagome lattice as a function of r_2/r_1 without long-range couplings. Panel (b) presents the case of $r_2/r_1 = 0.58$. Besides the three bulk bands (D), there are two edge bands (B and C) and six type I corner modes (A). B and C respectively represent the edge modes in the edges and the interior of edge bands. [(c)–(e)] Spatial distributions of the modes respectively in A, C, and B. [(f)–(j)] Same as panels [(a)–(e)] but with long-range couplings. B turns into the type II corner modes arising from long-range interactions. (k) Sum of the LDOS over all lattice sites, with long-range couplings. [(l)–(o)] Spatial distributions of LDOS integrated over an energy range respectively containing the type I and type II corner modes, edge bands, and bulk bands. Each site is represented as a circle with a radius proportional to the LDOS. The parameter is $r_2/r_1 = 0.58$. We assume 3% disorders in all couplings for showing robustness.

distributed at the two outmost sites of each corner [Fig. 5(c)]. As a result of the presence of long-range couplings, Figs. 5(f)–5(j) show that the 12 edge modes in the edges of the two edge bands turn into type II corner modes, maximally populated at six inside sites of each corner [Fig. 5(j)].

Figures 5(k)–5(o) exhibit that both the OBC energy spectrum and the topological corner modes can be detected by our introduced LDOS approach. As presented in Fig. 5(k), the distinct peaks in the sum of the LDOS $\rho(n, E_\alpha)$ over all sites precisely measure out the OBC energy spectrum in Fig. 5(g), including spectrally identifying the location of the type I and type II corner modes and the edge and bulk bands. Meanwhile, the integrations of the LDOS over an energy range covering the corner, edge, and bulk modes allows us to directly detect their spatial distributions, as plotted in Figs. 5(l)–5(o). As demonstrated, in addition to the six type I corner modes maximally located at the outmost corner sites, there also emerge 12 type II corner modes dominating at the inside corner sites, enabled by the long-range couplings. The considerable edge LDOS in Fig. 5(m) is attributed to the finite-size induced hybridization between the edge modes and the type II corner modes.

IV. SUMMARY AND OUTLOOK

In summary, our study reveals that ultracold-molecule trimerized Kagome optical-tweezer lattices exhibit significantly richer higher-order topological phases due to the long-range dipolar interactions. These long-range couplings induce diverse multiple corner modes at each corner, predominantly located at both the innermost and the outermost corner sites. Moreover, we have introduced a dynamic method for detecting spectral densities, enabling the differentiation of various corner modes at each corner. Our study underscores the benefits of utilizing reconfigurable optical-tweezer lattices and exploiting long-range molecular dipolar interactions to implement and enhance topological phases of matter.

Looking ahead, our research sets the stage for the exploration of interacting HOTPs as putting multiple spin-up excitation into the trimerized Kagome spin lattice [108,109]. Beyond the noninteracting HOTPs, delving into interacting HOTPs could provide deeper insights into the interplay between the interaction and the higher-order topology, allowing entirely unique topological properties to be uncovered. Moreover, as the numerical calculation of physical properties in two-dimensional interacting HOTPs surpasses the capabilities of current classical supercomputers, quantum simulation of interacting HOTPs also presents an exciting opportunity to attain a practical quantum advantage.

ACKNOWLEDGMENTS

This work was supported by the National Key Research and Development Program of China (Grant No. 2022YFA1404201), the National Natural Science Foundation of China (NSFC) (Grants No. 12034012, No. 12074234, and No. 12074231), the Changjiang Scholars and Innovative Research Team in University of Ministry of Education of China (PCSIRT)(IRT_17R70), the Fundamental Research Program of Shanxi Province (Grant No. 202303021223005), and the Fund for Shanxi 1331 Project Key Subjects Construction, 111 Project (D18001).

APPENDIX: THE DERIVATION OF BULK POLARIZATION

The momentum-space Hamiltonian for the long-range Kagome lattice model can be written as $H_k = H_0 + H_1$, where H_0 is the Hamiltonian without long-range couplings,

$$H_0 = \begin{pmatrix} 0 & J_1 + J_2 e^{i\vec{k}\cdot\vec{e}_1} & J_1 + J_2 e^{i\vec{k}\cdot\vec{e}_2} \\ J_1 + J_2 e^{-i\vec{k}\cdot\vec{e}_1} & 0 & J_1 + J_2 e^{-i\vec{k}\cdot\vec{e}_3} \\ J_1 + J_2 e^{-i\vec{k}\cdot\vec{e}_2} & J_1 + J_2 e^{i\vec{k}\cdot\vec{e}_3} & 0 \end{pmatrix}, \tag{A1}$$

and H_1 is the Hamiltonian describing the long-range couplings,

$$\begin{aligned} H_1 = {} & J_3 \begin{pmatrix} 0 & e^{i\vec{k}\cdot\vec{e}_3} + e^{i\vec{k}\cdot\vec{e}_2} & e^{i\vec{k}\cdot\vec{e}_1} + e^{-i\vec{k}\cdot\vec{e}_3} \\ e^{-i\vec{k}\cdot\vec{e}_3} + e^{-i\vec{k}\cdot\vec{e}_2} & 0 & e^{-i\vec{k}\cdot\vec{e}_1} + e^{i\vec{k}\cdot\vec{e}_2} \\ e^{-i\vec{k}\cdot\vec{e}_1} + e^{i\vec{k}\cdot\vec{e}_3} & e^{i\vec{k}\cdot\vec{e}_1} + e^{-i\vec{k}\cdot\vec{e}_2} & 0 \end{pmatrix} + 2J_4[\cos(\vec{k}\cdot\vec{e}_1) + \cos(\vec{k}\cdot\vec{e}_2) + \cos(\vec{k}\cdot\vec{e}_3)]\cdot I \\ & + J_5 \begin{pmatrix} 0 & e^{i\vec{k}\cdot(\vec{e}_2+\vec{e}_1)} + e^{-i\vec{k}\cdot(\vec{e}_3+\vec{e}_1)} & e^{i\vec{k}\cdot(\vec{e}_2+\vec{e}_1)} + e^{-i\vec{k}\cdot(-\vec{e}_3+\vec{e}_2)} \\ e^{-i\vec{k}\cdot(\vec{e}_2+\vec{e}_1)} + e^{i\vec{k}\cdot(\vec{e}_3+\vec{e}_1)} & 0 & e^{-i\vec{k}\cdot(-\vec{e}_3+\vec{e}_2)} + e^{i\vec{k}\cdot(\vec{e}_3+\vec{e}_1)} \\ e^{-i\vec{k}\cdot(\vec{e}_2+\vec{e}_1)} + e^{i\vec{k}\cdot(-\vec{e}_3+\vec{e}_2)} & e^{i\vec{k}\cdot(-\vec{e}_3+\vec{e}_2)} + e^{-i\vec{k}\cdot(\vec{e}_3+\vec{e}_1)} & 0 \end{pmatrix}. \end{aligned} \tag{A2}$$

Here $\vec{e}_{1,2} = (\pm\vec{e}_x + \sqrt{3}\vec{e}_y)/2$, $\vec{e}_3 = \vec{e}_x$, and I is the identity matrix. From the above Bloch Hamiltonian, one can obtain the nth band Bloch wave function $|u_{k,n}\rangle$ at the high-symmetry point K. The C_3 rotation symmetry operator is defined as

$$R_3 = \begin{pmatrix} 0 & 0 & 1 \\ 1 & 0 & 0 \\ 0 & 1 & 0 \end{pmatrix}. \tag{A3}$$

Then, using the formula $\theta_n(K) = \langle u_{K,n}|R_3|u_{K,n}\rangle$, we can extract the polarization associated with each Bloch band.

[1] N. Goldman, J. C. Budich, and P. Zoller, Nat. Phys. **12**, 639 (2016).

[2] D.-W. Zhang, Y.-Q. Zhu, Y. X. Zhao, H. Yan, and S.-L. Zhu, Adv. Phys. **67**, 253 (2018).

[3] N. R. Cooper, J. Dalibard, and I. B. Spielman, Rev. Mod. Phys. **91**, 015005 (2019).

[4] S. L. Zhu, H. Fu, C. J. Wu, S. C. Zhang, and L. M. Duan, Phys. Rev. Lett. **97**, 240401 (2006).

[5] L. B. Shao, S.-L. Zhu, L. Sheng, D. Y. Xing, and Z. D. Wang, Phys. Rev. Lett. **101**, 246810 (2008).

[6] C. Wang, C. Gao, C.-M. Jian, and H. Zhai, Phys. Rev. Lett. **105**, 160403 (2010).

[7] Y.-J. Lin, K. Jiménez-García, and I. B. Spielman, Nature (London) **471**, 83 (2011).

[8] P. Wang, Z.-Q. Yu, Z. Fu, J. Miao, L. Huang, S. Chai, H. Zhai, and J. Zhang, Phys. Rev. Lett. **109**, 095301 (2012).

[9] J. Y. Zhang, S.-C. Ji, Z. Chen, L. Zhang, Z.-D. Du, B. Yan, G.-S. Pan, B. Zhao, Y.-J. Deng, H. Zhai, S. Chen, and J.-W. Pan, Phys. Rev. Lett. **109**, 115301 (2012).

[10] L. W. Cheuk, A. T. Sommer, Z. Hadzibabic, T. Yefsah, W. S. Bakr, and M. W. Zwierlein, Phys. Rev. Lett. **109**, 095302 (2012).

[11] X.-J. Liu, Z.-X. Liu, and M. Cheng, Phys. Rev. Lett. **110**, 076401 (2013).

[12] X.-J. Liu, K. T. Law, and T. K. Ng, Phys. Rev. Lett. **112**, 086401 (2014).

[13] L. Huang, Z. Meng, P. Wang, P. Peng, S. Zhang, L. Chen, D. Li, Q. Zhou, and J. Zhang, Nat. Phys. **12**, 540 (2016).

[14] Z. Meng, L. Huang, P. Peng, D. Li, L. Chen, Y. Xu, C. Zhang, P. Wang, and J. Zhang, Phys. Rev. Lett. **117**, 235304 (2016).

[15] S.-G. Peng, C.-X. Zhang, S. Tan, and K. Jiang, Phys. Rev. Lett. **120**, 060408 (2018).

[16] D. Zhang, T. Gao, P. Zou, L. Kong, R. Li, X. Shen, X.-L. Chen, S.-G. Peng, M. Zhan, H. Pu, and K. Jiang, Phys. Rev. Lett. **122**, 110402 (2019).

[17] J. Dalibard, F. Gerbier, G. Juzeliūnas, and P. Öhberg, Rev. Mod. Phys. **83**, 1523 (2011).

[18] N. Goldman, G. Juzeliūnas, P. Öhberg, and I. B. Spielman, Rep. Prog. Phys. **77**, 126401 (2014).

[19] Y. Li, J. Zhang, Y. Wang, H. Du, J. Wu, W. Liu, F. Mei, J. Ma, L. Xiao, and S. Jia, Light: Sci. Appl. **11**, 13 (2022).

[20] M. Atala, M. Aidelsburger, J. T. Barreiro, D. Abanin, T. Kitagawa, E. Demler, and I. Bloch, Nat. Phys. **9**, 795 (2013).

[21] D.-W. Wang, R.-B. Liu, S.-Y. Zhu, and M. O. Scully, Phys. Rev. Lett. **114**, 043602 (2015).

[22] E. J. Meier, F. A. An, and B. Gadway, Nat. Commun. **7**, 13986 (2016).

[23] B. Song, L. Zhang, C. He, T. F. J. Poon, E. Hajiyev, S. Zhang, X.-J. Liu, and G.-B. Jo, Sci. Adv. **4**, eaao4748 (2018).

[24] E. J. Meier, F. A. An, A. Dauphin, M. Maffei, P. Massignan, T. L. Hughes, and B. Gadway, Science **362**, 929 (2018).

[25] Y. Li, H. Cai, D.-W. Wang, L. Li, J. Yuan, and W. Li, Phys. Rev. Lett. **124**, 140401 (2020).

[26] G. H. Reid, M. Lu, A. R. Fritsch, A. M. Piñeiro, and I. B. Spielman, Phys. Rev. Lett. **129**, 123202 (2022).

[27] M. Aidelsburger, M. Lohse, C. Schweizer, M. Atala, J. T. Barreiro, S. Nascimbène, N. R. Cooper, I. Bloch, and N. Goldman, Nat. Phys. **11**, 162 (2015).

[28] G. Jotzu, M. Messer, R. Desbuquois, M. Lebrat, T. Uehlinger, D. Greif, and T. Esslinger, Nature (London) **515**, 237 (2014).

[29] Z. Wu, L. Zhang, W. Sun, X.-T. Xu, B.-Z. Wang, S.-C. Ji, Y. Deng, S. Chen, X.-J. Liu, and J.-W. Pan, Science **354**, 83 (2016).

[30] W. Sun, B.-Z. Wang, X.-T. Xu, C.-R. Yi, L. Zhang, Z. Wu, Y. Deng, X.-J. Liu, S. Chen, and J.-W. Pan, Phys. Rev. Lett. **121**, 150401 (2018).

[31] B. Song, C. He, S. Niu, L. Zhang, Z. Ren, X.-J. Liu, and G.-B. Jo, Nat. Phys. **15**, 911 (2019).

[32] Z.-Y. Wang, X.-C. Cheng, B.-Z. Wang, J.-Y. Zhang, Y.-H. Lu, C.-R. Yi, S. Niu, Y. Deng, X.-J. Liu, S. Chen, and J.-W. Pan, Science **372**, 271 (2021).

[33] K. Wintersperger, C. Braun, F. N. Ünal, A. Eckardt, M. Di Liberto, N. Goldman, I. Bloch, and M. Aidelsburger, Nat. Phys. **16**, 1058 (2020).

[34] D. Xie, T.-S. Deng, T. Xiao, W. Gou, T. Chen, W. Yi, and B. Yan, Phys. Rev. Lett. **124**, 050502 (2020).

[35] X. Xu, J. Wang, J. Dai, R. Mao, H. Cai, S.-Y. Zhu, and D.-W. Wang, Rev. Lett. **129**, 273603 (2022).

[36] J.-Y. Zhang, C.-R. Yi, L. Zhang, R.-H. Jiao, K.-Y. Shi, H. Yuan, W. Zhang, X.-J. Liu, S. Chen, and J.-W. Pan, Phys. Rev. Lett. **130**, 043201 (2023).

[37] L. Duca, T. Li, M. Reitter, I. Bloch, M. Schleier-Smith, and U. Schneider, Science **347**, 288 (2015).

[38] N. Fläschner, B. S. Rem, M. Tarnowski, D. Vogel, D.-S. Lühmann, K. Sengstock, and C. Weitenberg, Science **352**, 1091 (2016).

[39] N. Fläschner, D. Vogel, M. Tarnowski, B. S. Rem, D.-S. Lühmann, M. Heyl, J. C. Budich, L. Mathey, K. Sengstock, and C. Weitenberg, Nat. Phys. **14**, 265 (2018).

[40] A. M. Kaufman and K. K. Ni, Nat. Phys. **17**, 1324 (2021).

[41] T. Langen, G. Valtolina, D. Wang, and J. Ye, Nat. Phys. **20**, 702 (2024).

[42] L. R. Liu, J. D. Hood, Y. Yu, J. T. Zhang, N. R. Hutzler, T. Rosenband, and K. K. Ni, Science **360**, 900 (2018).

[43] J. A. Blackmore, L. Caldwell, P. D. Gregory, E. M. Bridge, R. Sawant, J. Aldegunde, J. Mur-Petit, D. Jaksch, J. M. Hutson, B. E. Sauer, M. R. Tarbutt, and S. L. Cornish, Quantum Sci. Technol. **4**, 014010 (2019).

[44] L. R. Liu, J. D. Hood, Y. Yu, J. T. Zhang, K. Wang, Y. W. Lin, T. Rosenband, and K. K. Ni, Phys. Rev. X **9**, 021039 (2019).

[45] L. Anderegg, L. W. Cheuk, Y. Bao, S. Burchesky, W. Ketterle, K. K. Ni, and J. M. Doyle, Science **365**, 1156 (2019).

[46] J. T. Zhang, Y. Yu, W. B. Cairncross, K. Wang, L. R. B. Picard, J. D. Hood, Y. W. Lin, J. M. Hutson, and K. K. Ni, Phys. Rev. Lett. **124**, 253401 (2020).

[47] J. D. Hood, Y. Yu, Y. W. Lin, J. T. Zhang, K. Wang, L. R. Liu, B. Gao, and K. K. Ni, Phys. Rev. Res. **2**, 023108 (2020).

[48] L. W. Cheuk, L. Anderegg, Y. Bao, S. Burchesky, S. S. Yu, W. Ketterle, K. K. Ni, and J. M. Doyle, Phys. Rev. Lett. **125**, 043401 (2020).

[49] X. He, K. Wang, J. Zhuang, P. Xu, X. Gao, R. Guo, C. Sheng, M. Liu, J. Wang, J. Li, G. V. Shlyapnikov, and M. Zhan, Science **370**, 331 (2020).

[50] W. B. Cairncross, J. T. Zhang, L. R. B. Picard, Y. Yu, K. Wang, and K. K. Ni, Phys. Rev. Lett. **126**, 123402 (2021).

[51] S. Burchesky, L. Anderegg, Y. Bao, S. S. Yu, E. Chae, W. Ketterle, K. K. Ni, and J. M. Doyle, Phys. Rev. Lett. **127**, 123202 (2021).

[52] Y. Yu, K. Wang, J. D. Hood, L. R. B. Picard, J. T. Zhang, W. B. Cairncross, J. M. Hutson, R. Gonzalez-Ferez, T. Rosenband, and K. K. Ni, Phys. Rev. X **11**, 031061 (2021).

[53] L. Anderegg, S. Burchesky, Y. Bao, S. S. Yu, T. Karman, E. Chae, K. K. Ni, W. Ketterle, and J. M. Doyle, Science **373**, 779 (2021).

[54] M. Sroczyńska, A. Dawid, M. Tomza, Z. Idziaszek, T. Calarco, and K. Jachymski, New J. Phys. **24**, 015001 (2022).

[55] J. T. Zhang, L. R. B. Picard, W. B. Cairncross, K. Wang, Y. Yu, F. Fang, and K. K. Ni, Quantum Sci. Technol. **7**, 035006 (2022).

[56] K. Wang, C. P. Williams, L. R. B. Picard, N. Y. Yao, and K.-K. Ni, PRX Quantum **3**, 030339 (2022).

[57] C. Zhang and M. R. Tarbutt, PRX Quantum **3**, 030340 (2022).

[58] F. Deng, X.-Y. Chen, X.-Y. Luo, W. Zhang, S. Yi, and T. Shi, Phys. Rev. Lett. **130**, 183001 (2023).

[59] D. K. Ruttley, A. Guttridge, S. Spence, R. C. Bird, C. R. Le Sueur, J. M. Hutson, and S. L. Cornish, Phys. Rev. Lett. **130**, 223401 (2023).

[60] A. Guttridge, D. K. Ruttley, A. C. Baldock, R. González-Férez, H. R. Sadeghpour, C. S. Adams, and S. L. Cornish, Phys. Rev. Lett. **131**, 013401 (2023).

[61] C. Zhang, P. Yu, A. Jadbabaie, and N. R. Hutzler, Phys. Rev. Lett. **131**, 193602 (2023).

[62] Y. Lu, S. J. Li, C. M. Holland, and L. W. Cheuk, Nat. Phys. **20**, 389 (2024).

[63] P. D. Gregory, L. M. Fernley, A. L. Tao, S. L. Bromley, J. Stepp, Z. Zhang, S. Kotochigova, K. R. Hazzard, and S. L. Cornish, Nat. Phys. **20**, 415 (2024).

[64] Y. Bao, S. S. Yu, J. You, L. Anderegg, E. Chae, W. Ketterle, K.-K. Ni, and J. M. Doyle, arXiv:2309.08706.

[65] D. DeMille, Phys. Rev. Lett. **88**, 067901 (2002).

[66] A. André, D. DeMille, J. M. Doyle, M. D. Lukin, S. E. Maxwell, P. Rabl, R. J. Schoelkopf, and P. Zoller, Nat. Phys. **2**, 636 (2006).

[67] S. F. Yelin, K. Kirby, and R. Côté, Phys. Rev. A **74**, 050301(R) (2006).

[68] E. Charron, P. Milman, A. Keller, and O. Atabek, Phys. Rev. A **75**, 033414 (2007).

[69] K. K. Ni, T. Rosenband, and D. D. Grimes, Chem. Sci. **9**, 6830 (2018).

[70] M. Hughes, M. D. Frye, R. Sawant, G. Bhole, J. A. Jones, S. L. Cornish, M. R. Tarbutt, J. M. Hutson, D. Jaksch, and J. Mur-Petit, Phys. Rev. A **101**, 062308 (2020).

[71] R. Sawant, J. A. Blackmore, P. D. Gregory, J. Mur-Petit, D. Jaksch, J. Aldegunde, J. M. Hutson, M. R. Tarbutt, and S. L. Cornish, New J. Phys. **22**, 013027 (2020).

[72] A. Micheli, G. K. Brennen, and P. Zoller, Nat. Phys. **2**, 341 (2006).

[73] R. Barnett, D. Petrov, M. D. Lukin, and E. Demler, Phys. Rev. Lett. **96**, 190401 (2006).

[74] H. P. Büchler, A. Micheli, and P. Zoller, Nat. Phys. **3**, 726 (2007).

[75] A. V. Gorshkov, S. R. Manmana, G. Chen, J. Ye, E. Demler, M. D. Lukin, and A. M. Rey, Phys. Rev. Lett. **107**, 115301 (2011).

[76] A. V. Gorshkov, S. R. Manmana, G. Chen, E. Demler, M. D. Lukin, and A. M. Rey, Phys. Rev. A **84**, 033619 (2011).

[77] M. A. Baranov, M. Dalmonte, G. Pupillo, and P. Zoller, Chem. Rev. **112**, 5012 (2012).

[78] K. R. A. Hazzard, S. R. Manmana, M. Foss-Feig, and A. M. Rey, Phys. Rev. Lett. **110**, 075301 (2013).

[79] B. Yan, S. A. Moses, B. Gadway, J. P. Covey, K. R. A. Hazzard, A. M. Rey, D. S. Jin, and J. Ye, Nature (London) **501**, 521 (2013).

[80] K. R. A. Hazzard, B. Gadway, M. Foss-Feig, B. Yan, S. A. Moses, J. P. Covey, N. Y. Yao, M. D. Lukin, J. Ye, D. S. Jin, and A. M. Rey, Phys. Rev. Lett. **113**, 195302 (2014).

[81] N. Y. Yao, M. P. Zaletel, D. M. Stamper-Kurn, and A. Vishwanath, Nat. Phys. **14**, 405 (2018).

[82] R. V. Krems, Phys. Chem. Chem. Phys. **10**, 4079 (2008).

[83] L. D. Carr, D. DeMille, R. V. Krems, and J. Ye, New J. Phys. **11**, 055049 (2009).

[84] N. Balakrishnan, J. Chem. Phys. **145**, 150901 (2016).

[85] J. L. Bohn, M. Rey, and J. Ye, Science **357**, 1002 (2017).

[86] S. A. Moses, J. P. Covey, M. T. Miecnikowski, D. S. Jin, and J. Ye, Nat. Phys. **13**, 13 (2017).

[87] M. S. Safronova, D. Budker, D. DeMille, D. F. J. Kimball, A. Derevianko, and C. W. Clark, Rev. Mod. Phys. **90**, 025008 (2018).

[88] C. Chin, V. V. Flambaum, and M. G. Kozlov, New J. Phys. **11**, 055048 (2009).

[89] Y. Bao, S. S. Yu, L. Anderegg, E. Chae, W. Ketterle, K.-K. Ni, and J. M. Doyle, Science **382**, 1138 (2023).

[90] C. M. Holland, Y. Lu, and L. W. Cheuk, Science **382**, 1143 (2023).

[91] N. Y. Yao, C. R. Laumann, A. V. Gorshkov, S. D. Bennett, E. Demler, P. Zoller, and M. D. Lukin, Phys. Rev. Lett. **109**, 266804 (2012).

[92] D. Peter, N. Y. Yao, N. Lang, S. D. Huber, M. D. Lukin, and H. P. Buchler, Phys. Rev. A **91**, 053617 (2015).

[93] N. Y. Yao, A. V. Gorshkov, C. R. Laumann, A. M. Laüchli, J. Ye, and M. D. Lukin, Phys. Rev. Lett. **110**, 185302 (2013).

[94] S. V. Syzranov, M. L. Wall, B. Zhu, V. Gurarie, and A. M. Rey, Nat. Commun. **7**, 13543 (2016).

[95] T. Schuster, F. Flicker, M. Li, S. Kotochigova, J. E. Moore, J. Ye, and N. Y. Yao, Phys. Rev. A **103**, 063322 (2021).

[96] T. Schuster, F. Flicker, M. Li, S. Kotochigova, J. E. Moore, J. Ye, and N. Y. Yao, Phys. Rev. Lett. **127**, 015301 (2021).

[97] J. Jiang, J.-H. Zhang, F. Mei, Z. Ji, Y. Hu, J. Ma, L. Xiao, and S. Jia, Phys. Rev. A **106**, 023318 (2022).

[98] S. de Léséleuc, V. Lienhard, P. Scholl, D. Barredo, S. Weber, N. Lang, H. P. Büchler, T. Lahaye, and A. Browaeys, Science **365**, 775 (2019).

[99] C. P. Liang, Y. Liu, F.-F. Li, S. W. Leung, Y. Poo, and J.-H. Jiang, Phys. Rev. Appl. **20**, 034028 (2023).

[100] D.-W. Zhang, F. Mei, Z.-Y. Xue, S.-L. Zhu, and Z. D. Wang, Phys. Rev. A **92**, 013612 (2015).

[101] Y. Liu, S. Leung, F. F. Li, Z. K. Lin, X. Tao, Y. Poo, and J. H. Jiang, Nature (London) **589**, 381 (2021).

[102] W. A. Benalcazar, B. A. Bernevig, and T. L. Hughes, Science **357**, 61 (2017).

[103] F. Schindler, A. M. Cook, M. G. Vergniory, Z. Wang, S. S. P. Parkin, B. A. Bernevig, and T. Neupert, Sci. Adv. **4**, eaat0346 (2018).

[104] M. Ezawa, Phys. Rev. B **98**, 201402(R) (2018).

[105] C. Fang, M. J. Gilbert, and B. A. Bernevig, Phys. Rev. B **86**, 115112 (2012).

[106] M. Ezawa, Phys. Rev. Lett. **120**, 026801 (2018).

[107] W. A. Benalcazar, T. Li, and T. L. Hughes, Phys. Rev. B **99**, 245151 (2019).

[108] Y. You, T. Devakul, F. J. Burnell, and T. Neupert, Phys. Rev. B **98**, 235102 (2018).

[109] O. Dubinkin and T. L. Hughes, Phys. Rev. B **99**, 235132 (2019).